Banner appropriate to article type will appear here in typeset article

Vorticity cascade and turbulent drag in wall-bounded flows: plane Poiseuille flow

Samvit Kumar[1] †, Charles Meneveau[1] and Gregory Eyink[1,2]

[1]Department of Mechanical Engineering, The Johns Hopkins University, Baltimore, Maryland, USA

[2]Department of Applied Mathematics, The Johns Hopkins University, Baltimore, Maryland, USA

(Received xx; revised xx; accepted xx)

SUPPLEMENTARY MATERIALS

A. Quadrant contributions

Partial averages of the flux terms $v\omega_z - w\omega_y$, $v\omega_z$ and $-w\omega_y$ conditioned on "low speed ($u' < 0$)" and "high speed ($u' > 0$)" events are shown in Fig A.1a, A.1b and A.1c respectively. The plot in Fig A.1c shows that the stretching/tilting term ($-w\omega_y$) is agnostic to the sign of u' for $y^+ \lesssim 100$, where both low speed and high speed streaks produce up-gradient contributions. For $100 \lesssim y^+ \lesssim 500$ low speed streaks make down-gradient contributions while high speed streaks make up-gradient contributions to this stretching term. Close to the centerline ($y^+ \gtrsim 500$), both contributions are down-gradient. The convective term (shown in Fig A.1b), on the other hand, shows strongly opposing behaviours for low speed and high speed streaks across nearly the entire channel (for $y^+ \lesssim 700$), with low speed streaks making down-gradient contributions but high speed streaks up-gradient contributions. By contrast, both contributions to the convective flux are down-gradient close to the centerline ($y^+ \gtrsim 700$). The total nonlinear flux (shown in Fig A.1a), is dominated by the convective term and behaves similarly across most of the channel ($5 \lesssim y^+ \lesssim 700$), with low-speed streaks being down-gradient and high-speed streaks being up-gradient. Within the viscous sublayer($y^+ \lesssim 5$), low speed streaks make no contributions to the flux and the entire flux is due to high speed streaks. Close to the centerline ($y^+ \gtrsim 700$) both contributions are down-gradient. The observed correlations of the separate flux terms with u' are plausibly explained as a consequence of the primary correlation with v' due to Lighthill's mechanism and the secondary correlation of v' with u'.

This idea is illuminated by the quadrant correlations, discussed next. The contributions from the four individual quadrants of the $u'-v'$ plane (see Pope (2000)) are shown for the total nonlinear flux (Fig A.2a), the convection/advection term (Fig A.2b) and the stretching/tilting term (Fig A.2c). Contributions from "active (Q2+Q4)" and "inactive (Q1 +Q3)" motions are plotted as well. The latter show that active motions contribute nearly the entire flux for the convective term, while inactive motions make a much a smaller contribution (Fig A.2b). The stretching/tilting term is nearly agnostic to active/inactive motions for $y^+ \lesssim 30$ but also dominated by active motions for $y^+ \gtrsim 30$ (Fig A.2c). On the whole, the net nonlinear flux (Fig A.2a) is dominated by contributions from active motions, with inactive motions making

† Email address for correspondence: skumar67@jh.edu

Abstract must not spill onto p.2

a decidedly smaller contribution, and this effect is mainly through the convection term. These observations are consistent with our explanation above that the observed correlations of the flux contributions are due to the primary correlation with v' and the strong anti-correlation between u' and v' in $Q2+Q4$

Further evidence for this picture is provided by the separate quadrant contributions. From Fig A.2b for the convective term it may be seen that Q1 and Q2 where $v' > 0$ both make down-gradient contributions, while Q3 and Q4 where $v' < 0$ both make up-gradient contributions across the entire channel. On the other hand, the stretching/tilting term in Fig A.2c exhibits opposite flux directions across most of the channel, with Q1 and Q2 up-gradient and Q3 and Q4 down-gradient. Furthermore, for both convection and stretching terms, the $Q1$ correlations while similar to the $Q2$ correlations are smaller in magnitude,and likewise the $Q3$ correlations while similar to the $Q4$ correlations are smaller. This suggests again that the primary correlation is with v', but that the dominant contribution arises from the "active" quadrants $Q2+Q4$ where u' and v' are anti-correlated.

Altogether, these results support our claim that the correlation most relevant to the physics is that between the flux and regions of outflow ($v' > 0$) and inflow ($v' < 0$), as shown in Fig 7 in the main text. The dominance of the "active" regions produces a secondary correlation of vorticity flux with u'.

We note that contributions to vorticity flux from the four quadrants $Q1-Q4$ were calculated previously by Vidal *et al.* (2018), but for duct flow with sidewalls (both straight and curved) at two constant z planes. We cannot compare our results with theirs, not only because of the differences in the simulated flows but also because they considered products of fluctuating terms $v'\omega_z'$ and $w'\omega_y'$. Since $w\omega_y = w'\omega_y'$, our results for this term agree well with theirs for z away from sidewalls, but our results for $v\omega_z$ differ considerably from theirs for $v'\omega_z'$.

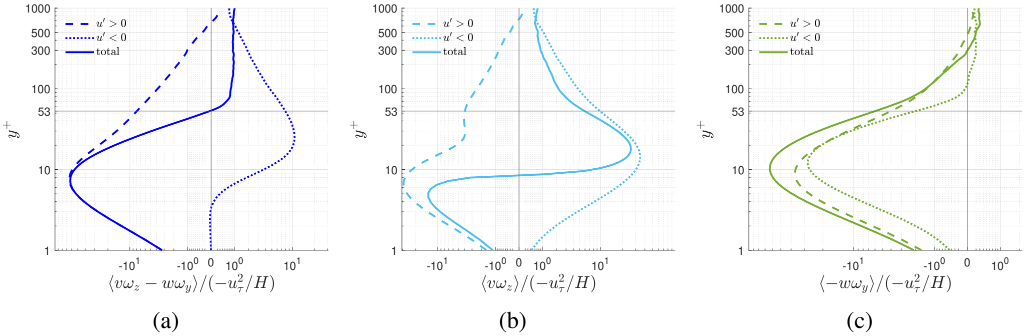

Figure A.1: Contributions from high speed streaks ($u' > 0$) and low speed streaks ($u' < 0$), to the (a) nonlinear flux, (b) convection/advection and (c) stretching/tilting, averaged over time and wall parallel planes, plotted as a function of wall distance.

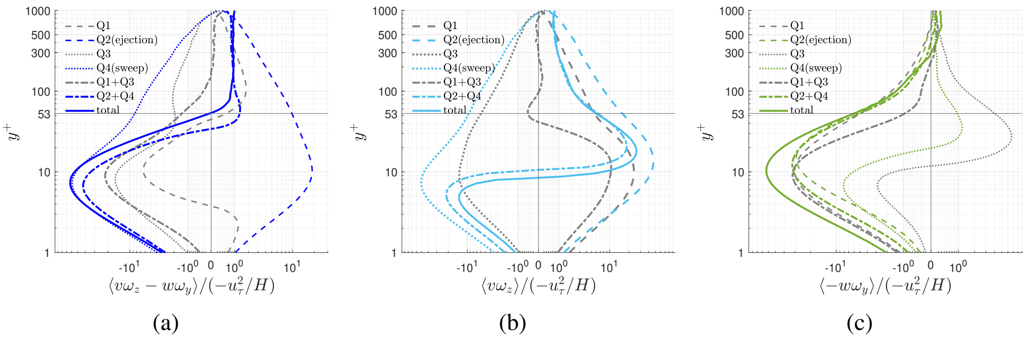

Figure A.2: Contributions from quadrants to the nonlinear flux (a), convection/advection (b) and stretching/tilting (c), averaged over time and wall parallel planes, plotted as a function of wall distance.

B. Comparison with data from Del Alamo *et al.* (2004)

We compare the spanwise two point velocity-vorticity correlations computed from channel flow data at $Re_\tau = 1000$ from the Johns Hopkins Turbulence Database Li *et al.* (2008); Graham *et al.* (2016) and at $Re_\tau = 934$ from Del Alamo *et al.* (2004) reported in Monty *et al.* (2011) in Fig B.3. The correlations are related to the respective spanwise co-spectra as follows:

$$R^+_{w\omega_y}(\Delta z) = \frac{R_{w\omega_y}(\Delta z)}{u_\tau^2/\delta_\nu} = \frac{1}{u_\tau^2/\delta_\nu}\int_0^\infty \phi_{w\omega_y}(k_z)e^{ik_z\Delta z}dk_z \tag{B.1}$$

$$R^+_{v\omega_z}(\Delta z) = \frac{R_{v\omega_z}(\Delta z)}{u_\tau^2/\delta_\nu} = \frac{1}{u_\tau^2/\delta_\nu}\int_0^\infty \phi_{v\omega_z}(k_z)e^{ik_z\Delta z}dk_z \tag{B.2}$$

We observe good agreement between correlations from both datasets.

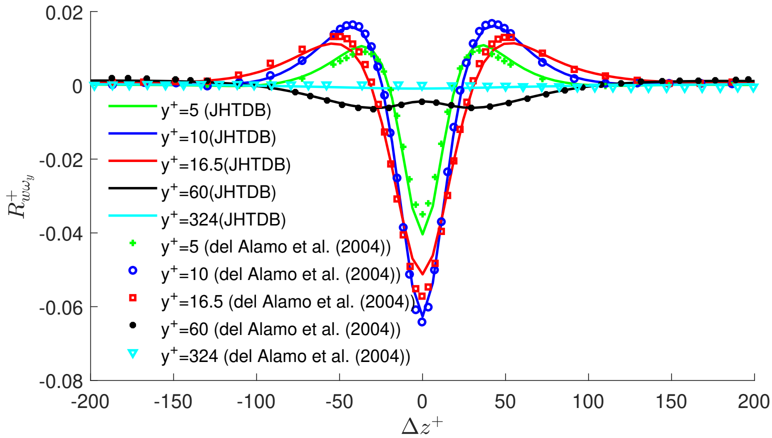

(a)

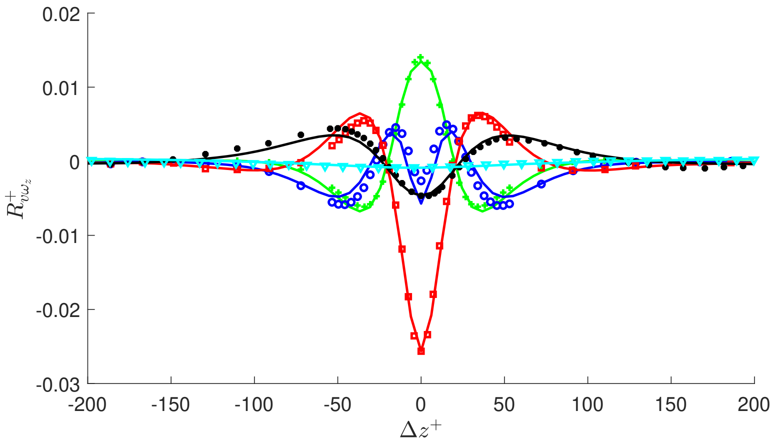

(b)

Figure B.3: Spanwise two-point correlation of (a) spanwise velocity and wall normal vorticity ($R^{+}_{w\,\omega_y}$), (b) spanwise vorticity and wall normal velocity ($R^{+}_{v\,\omega_z}$), computed from channel flow data at $Re_\tau = 1000$ from JHTDB(Graham *et al.* (2016)) and from earlier simulation data of channel flow at $Re_\tau = 934$ by Del Alamo *et al.* (2004) reported in Monty *et al.* (2011).

C. Velocity-vorticity co-spectra

The co-spectrum of nonlinear flux is given by $\phi_{v\omega_z} - \phi_{w\omega_y}$ with the spanwise co-spectra shown in Fig 8 and the streamwise cospectrum in Fig. 10 of the main text. The latter streamwise "net force spectra" have been the subject of detailed study in prior works of Guala *et al.* (2006); Balakumar & Adrian (2007); Wu *et al.* (2012). The wall-normal derivative of the Reynolds shear stress is characterized in these works as producing retardation of the mean flow above y_p and acceleration below, associated with a negative and a positive sign respectively. This retarding force is produced by a down-gradient flux of spanwise vorticity while an accelerating force results from an up-gradient flux, as discussed in Section 1. The detailed study by Wu *et al.* (2012) found large positive (accelerating) values for the streamwise net force spectrum concentrated below $y^+ = 20$, and observed that below the top of the buffer layer (at $y^+ = 30$), all scales except the very smallest ($\lambda_x < 0.15R$, $R^+ = 685$) accelerate the mean flow (or contribute an up-gradient flux). Conversely, for $y > 0.2R$, they found negative (decelerating or contributing a down-gradient flux) values for all scales. In the wall-normal region where $y^+ > 20$ and $y < 0.2R$, they found a complicated y variation of the spectra with negative (decelerating or with a down-gradient flux) values sandwiched between positive (decelerating or with an up-gradient flux) values, each occupying a varying range of scales. These observations mirror our own, as illustrated particularly by our Fig 10 .

In this section, we look at the constituent co-spectra, i.e., $\phi_{v\omega_z}$ and $-\phi_{w\omega_y}$, both spanwise and streamwise. All of the mean features of these 1D spectra can be inferred from the corresponding 2D cospectra plotted in Section E. However, we present the 1D cospectra here for completeness.

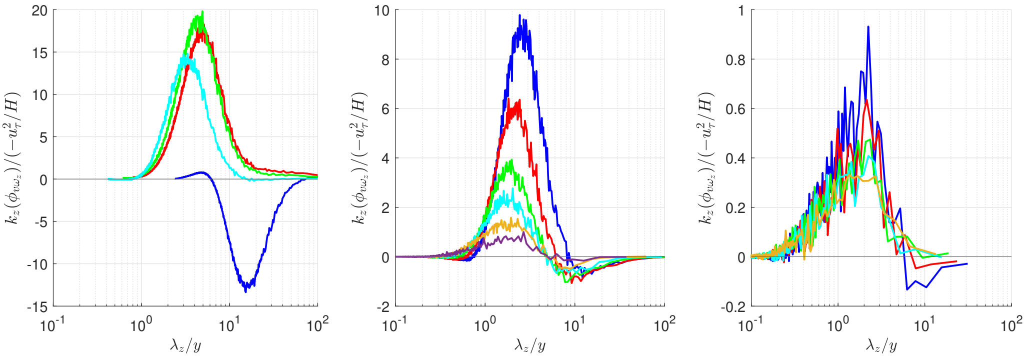

(a) Spanwise co-spectra: Viscous & Buffer Layers

(b) Spanwise co-spectra: Log Layer

(c) Spanwise co-spectra: Outer Layer

Figure C.4: Normalized spanwise cospectra of wall normal velocity- spanwise vorticity ($\phi_{v\omega_z}$), in the (a) viscous & buffer layers, (b) log layer and (c) outer layer. Curves have the same meaning as in corresponding plots in Fig 8.

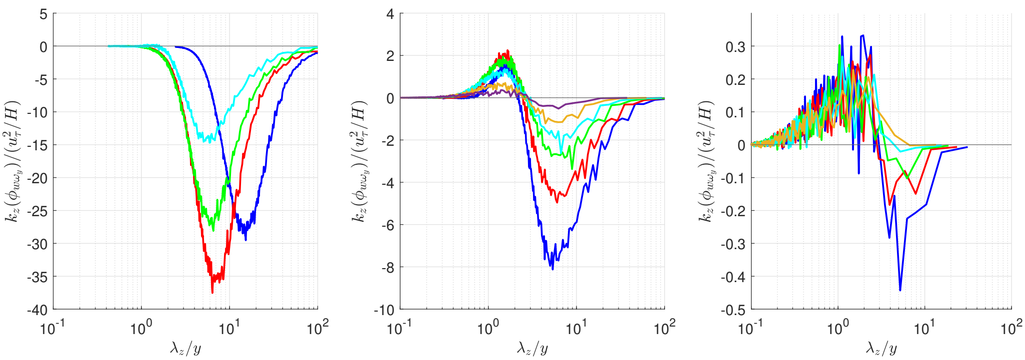

(a) Spanwise co-spectra: Viscous & Buffer Layer

(b) Spanwise co-spectra: Log Layer

(c) Spanwise co-spectra: Outer Layer

Figure C.5: Normalized spanwise cospectra of (negative of) the spanwise velocity - wall normal vorticity ($-\phi_{w\omega_y}$), in the (a) viscous & buffer layers, (b) log layer and (c) outer layer. Curves have the same meaning as in corresponding plots in Fig 8.

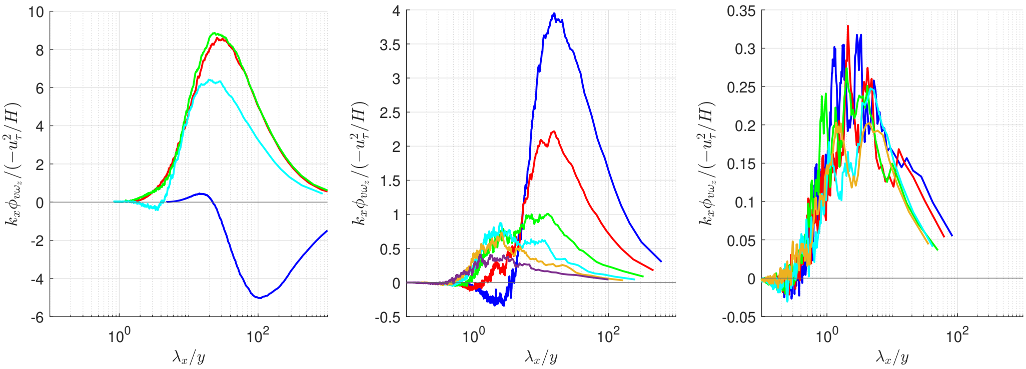

(a) Streamwise co-spectra: Viscous & Buffer Layers

(b) Streamwise co-spectra: Log Layer

(c) Streamwise co-spectra: Outer Layer

Figure C.6: Normalized streamwise cospectra of wall normal velocity- spanwise vorticity ($\phi_{v\omega_z}$), in the (a) viscous & buffer layers, (b) log layer and (c) outer layer. Curves have the same meaning as in corresponding plots in Fig 8.

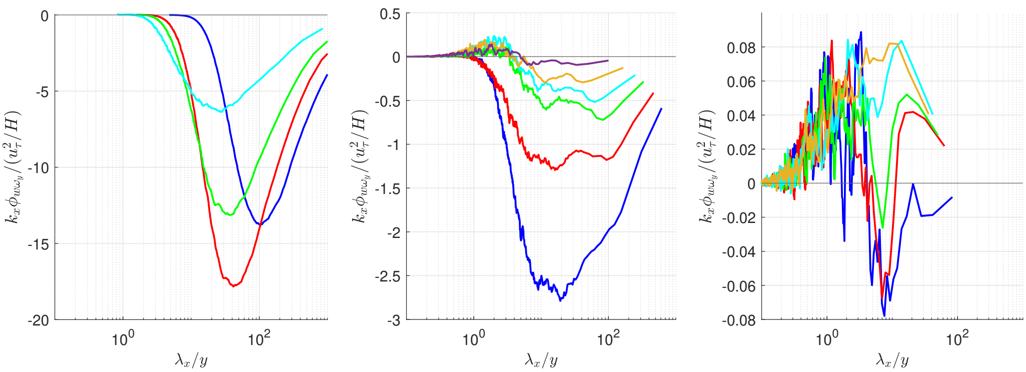

(a) Streamwise co-spectra: Viscous & Buffer Layers

(b) Streamwise co-spectra: Log Layer

(c) Streamwise co-spectra: Outer Layer

Figure C.7: Normalized streamwise cospectra of (negative of) the spanwise velocity - wall normal vorticity ($-\phi_{w\omega_y}$), in the (a) viscous & buffer layers, (b) log layer and (c) outer layer. Curves have the same meaning as in corresponding plots in Fig 8.

D. Smoothing of 2D Spectra

Since the 2D cospectra in this study were obtained by averaging over only 38 snapshots, we smooth the 2D co-spectra by a simple running average in Fourier space. Given that the streamwise and spanwise domain size is L_x and L_z, and the number of corresponding grid points are N_x and N_z (assuming both are even), the streamwise and spanwise wavenumbers are given by $k_i = 2\pi i/L_x$ and $k_j = 2\pi j/L_z$ where $i, j \in \mathbb{Z}$. We demonstrate the smoothing procedure by showing its application to obtain $\varphi_{v\omega_z}(k_i, k_j)$, where $i, j \in \{0, 1, 2, \ldots\}$ (shown in Fig E.10). We start by defining the relevant 2D Fourier transforms and the cospectrum as,

$$
\begin{aligned}
&\hat{v}(k_i, k_j, y) = FFT_{2D}[v(x, y, z)],\ \hat{\omega}_z(k_i, k_j, y) = FFT_{2D}[\omega_z(x, y, z)],\ \text{and} \\
&\Phi_{v\omega_z}(k_i, k_j, y) := \langle \hat{v}\hat{\omega}_z^* \rangle,\ \text{where},\ i = \{-N_x/2+1, -N_x/2+2, \ldots -1, 0, 1, ..N_x/2-1\}, \\
&j = \{-N_z/2+1, -N_z/2+2, \ldots -1, 0, 1, \ldots N_z/2-1\}\,.
\end{aligned} \tag{D.1}
$$

We extend the co-spectrum to the full wavenumber space by defining,

$$
\Phi_{v\omega_z}(k_i, k_j, y) := 0,\ \forall\, |i| \geqslant \frac{N_x}{2}, |j| \geqslant \frac{N_z}{2}. \tag{D.2}
$$

This spectrum satisfies the property,

$$
\sum_{i=-\infty}^{\infty}\sum_{j=-\infty}^{\infty} \Phi_{v\omega_z}(k_i, k_j, y)\Delta k_x \Delta k_z = \langle v\omega_z\rangle(y),\ where,\ \Delta k_x = \frac{2\pi}{L_x}, \Delta k_z = \frac{2\pi}{L_z}. \tag{D.3}
$$

We now introduce the smoothed co-spectrum, with streamwise window size $\delta k_x = 2b_x\Delta k_x$ and spanwise window size $\delta k_z = 2b_z\Delta k_z$ as,

$$
\Phi^{b_x,b_y}_{v\omega_z}(k_i, k_j, y) := \frac{1}{(2b_x+1)(2b_z+1)} \sum_{m=-b_x}^{b_x}\sum_{n=-b_z}^{b_z} \Phi_{v\omega_z}(k_{i+m}, k_{j+n}, y). \tag{D.4}
$$

This smoothing maintains the value of the integral over the full wavenumber space. We then add contributions reflected in the x- and z-axes so that the spectra depend only on wavenumber magnitudes $k_x \geqslant 0$, $k_z \geqslant 0$, yielding,

$$
\begin{aligned}
&\varphi_{v\omega_z}(k_i, k_j, y) := \Phi^{b_x,b_z}_{v\omega_z}(k_i, k_j, y) + \Phi^{b_x,b_z}_{v\omega_z}(-k_i, k_j, y) + \Phi^{b_x,b_z}_{v\omega_z}(-k_i, -k_j, y) + \\
&\Phi^{b_x,b_z}_{v\omega_z}(k_i, -k_j, y),\ i = \left\{0, 1, 2, \ldots, \frac{N_x}{2} + b_x - 1\right\},\ j = \left\{0, 1, 2, \ldots, \frac{N_z}{2} + b_z - 1\right\}.
\end{aligned} \tag{D.5}
$$

This single quadrant co-spectrum satisfies the relation,

$$
\sum_{i=0}^{\infty}\sum_{j=0}^{\infty} \varphi_{v\omega_z}(k_i, k_j, y)\Delta k_x \Delta k_z = \langle v\omega_z\rangle(y). \tag{D.6}
$$

To choose the appropriate window size $b_x = b_z = b$ we use the Principle of Minimal Sensitivity (Stevenson 1981). For this purpose, we calculate the L^2 distances between cospectra filtered with consecutive window sizes $(||\Phi^{b+1,b+1}_{v\omega_z - w\omega_y} - \Phi^{b,b}_{v\omega_z - w\omega_y}||_2, b = 0, 1, 2, \ldots)$ and plot these versus b in Fig D.8. We find that the distance is least sensitive to window size for $2 \geqslant b \geqslant 4$, so that we keep the window size at $b = 3$ for all 2D cospectra plotted in the main text. Raw co-spectra, as well as those smoothed with two window sizes, $b = 3$ and $b = 6$, are plotted in Fig D.9. We observe that smoothing the co-spectra removes some of the high wavenumber noise present in the un-smoothed spectrum (Fig D.9a). Increasing the window size beyond $b = 3$ (Fig D.9b) does not lead to any appreciable noise reduction but begins to smear out larger scale features (Fig D.9c)

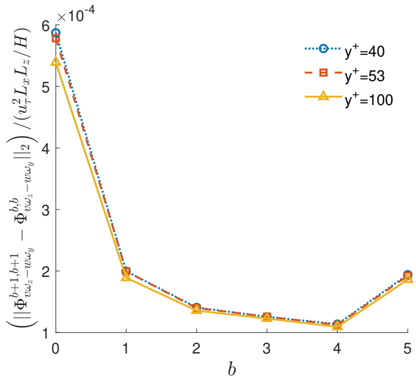

Figure D.8: The L^2 distance between co-spectra filtered with consecutive window sizes. We select $w_x = w_z = 3$ for all 2D co-spectra, based on the Principle of minimal sensitivity (see Stevenson (1981)).

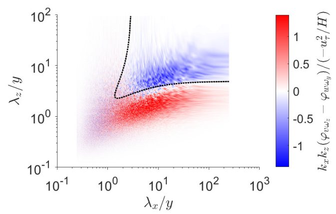

(a) Without smoothing

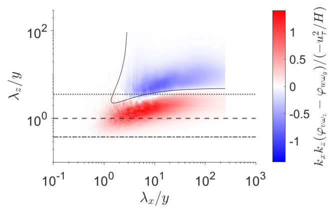

(b) $b_x = b_z = 3$

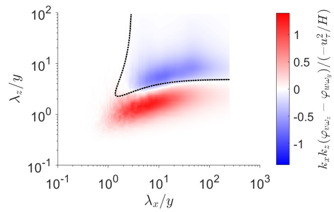

(c) $w_x = w_z = 6$

Figure D.9: Normalized 2D co-spectra of the nonlinear flux $(\varphi_{v\omega_z} - \varphi_{w\omega_y})$ at $y^+ = 100$. The co-spectra ahown are (a) unsmoothed , smoothed with window size (b) $b_x = b_z = 3$, and (c) $b_x = b_z = 6$. The black dashed curves mark iso-contour of the filter $\mathcal{D}(k_x, k_z, y) = 0.5$, described in Appendix F. Smoothing removes some of the high wavenumber noise seen in (a).

E. Individual Velocity-Vorticity 2D Cospectra

Corresponding to the 2D flux cospectra shown in Fig 11 of the main text, we plot the separate 2D cospectra for the advective flux ($\varphi_{v\omega_z}(k_x, k_z, y)$) and stretching flux ($-\varphi_{w\omega_y}(k_x, k_z, y)$), in Fig E.10 and Fig E.11, respectively. These cospectra have a bipartite structure similar to the total nonlinear flux cospectra plotted in Fig 11. However, the advective flux cospectra (Fig E.10) make a largely down-gradient contribution, while the stretching flux cospectra (Fig E.11) make a largely up-gradient contribution to the total nonlinear flux. An exception to this trend is marked by the cospectra at $y^+ \lesssim 10$, where both contributions are up-gradient and $y^+ \gtrsim 500$ where both are down-gradient. Therefore, we can say that, by and large, the advective flux makes a down-gradient contribution while the stretching flux makes an up-gradient contribution to the nonlinear flux co-spectra, for $10 \lesssim y^+ \lesssim 500$.

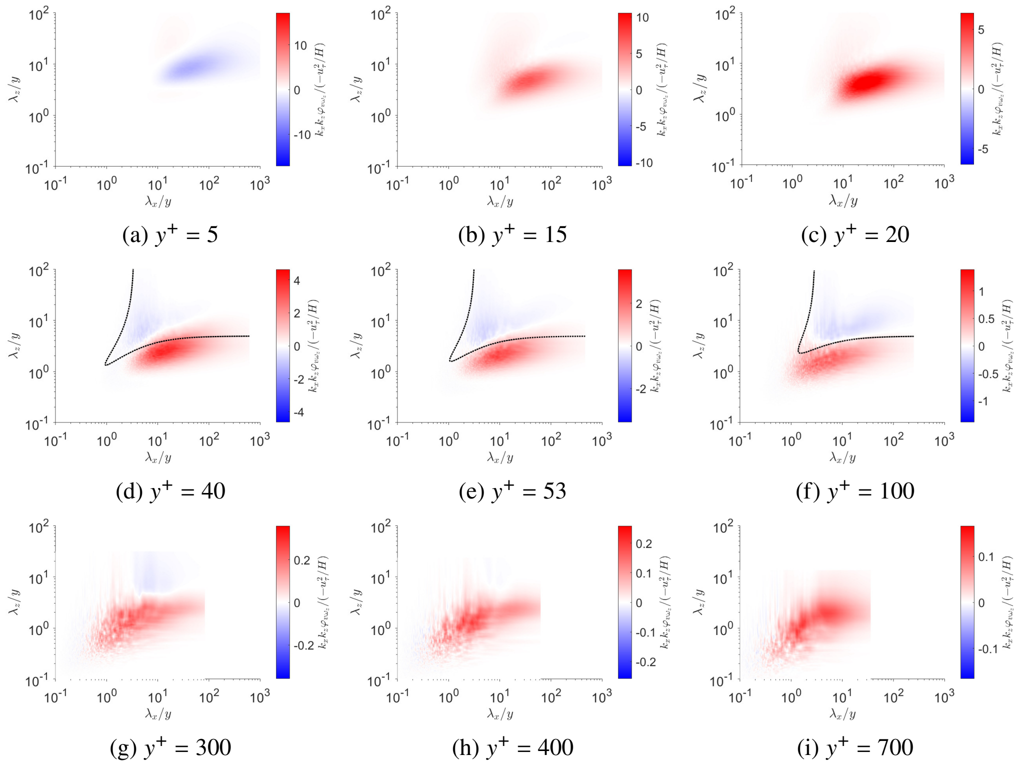

Figure E.10: Normalized 2D co-spectra of the convective term ($\varphi_{v\omega_z}$), in the viscous & buffer layers (a,b,c), log layer (d,e,f) and outer layer (g,h,i).The black dashed curves mark iso-contour of the filter $\mathcal{D}(k_x, k_z, y) = 0.5$, described in Appendix F.

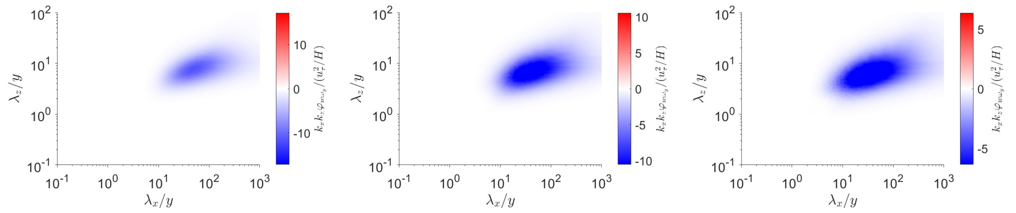

(a) $y^+ = 5$ (b) $y^+ = 15$ (c) $y^+ = 20$

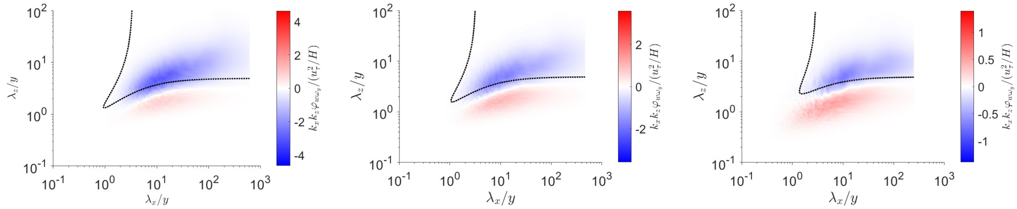

(d) $y^+ = 40$ (e) $y^+ = 53$ (f) $y^+ = 100$

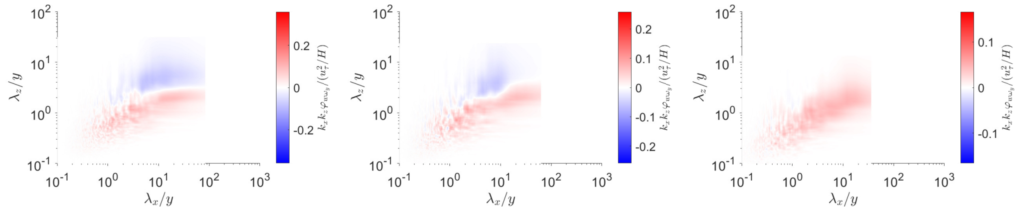

(g) $y^+ = 300$ (h) $y^+ = 400$ (i) $y^+ = 700$

Figure E.11: Normalized 2D co-spectra of the stretching/tilting term $(-\varphi_{w\omega_y})$, in the viscous & buffer layers (a,b,c), log layer (d,e,f) and outer layer (g,h,i).The black dashed curves mark iso-contour of the filter $\mathcal{D}(k_x, k_z, y) = 0.5$, described in Appendix F.

F. Dragonfly Filter

The 2D nonlinear flux cospectra shown in Fig 11, particularly in the log layer, possess a natural "boundary" in wave number space separating regions of down-gradient and up-gradient transport . In this section, we propose a simple filter that allows us to distinguish the two competing scales in the log layer. We chose the filter kernel to be graded in order to reduce Gibbs-type oscillations in the spatial filtered fields. A simple choice which we dub the "dragonfly" filter ($\mathcal{D}$) is a product of two Gaussian filters. To capture the spectral region of interest, the two Gaussians are chosen to have elliptical level curves centered at the origin with principal axes of respective slopes $\pm m$:

$$\mathcal{D}(k_x, k_z, y) := \exp\left(-\left[\frac{(|k_x| + m|k_z|)^2}{k_a^2} + \frac{(|k_z| - m|k_x|)^2}{k_b^2}\right]\right) \tag{F.1}$$

We then define also a complement filter ($\mathcal{D}^c := 1 - \mathcal{D}$). To choose the optimum parameters m, k_a^+ and k_b^+, we minimize the flux value Σ_{yz}^U (largest negative value) separately for each $y^+ = 40, 60, 80, ...300$. However, for computational convenience, it is useful to have an explicit representation of these optimum parameters as functions of y. The optimum values are shown in Fig F.12 and may be reasonably described by power laws. In fact, the optimum k_b fits a y^{-1} power law (shown in Fig F.12c) very well. Parameters m and k_a are not represented as well by power laws and show a "kink" around $y^+ = 100$, which can be a subject of further investigation. The best fits by power laws yield

$$m = 1.56(y^+)^{-0.22}, \tag{F.2}$$

$$k_a^+ = 92.76(y^+)^{-1.56}, \tag{F.3}$$

$$k_b^+ = 1.49(y^+)^{-0.99}. \tag{F.4}$$

which are plotted also in Fig F.12. These power-law relations were deemed adequate and have been used for the results presented in the paper.

The velocity and vorticity fields are filtered using $\mathcal{D}(k_x, k_z, y)$ and $\mathcal{D}^c(k_x, k_z, y)$ yielding the up-gradient and down-gradient parts of the fields respectively. The procedure to obtain the filtered fields (q^U and q^D) from an unfiltered field q, at a given wall distance y, is as follows:

$$\hat{q}(k_x, k_z, y) = FFT_{2D}[q(x, y, z)] \tag{F.5}$$

$$q^U(x, y, z) = iFFT_{2D}[\mathcal{D}(k_x, k_z, y)\hat{q}(k_x, k_z, y)], \tag{F.6}$$

$$q^D(x, y, z) = iFFT_{2D}[\mathcal{D}^c(k_x, k_z, y)\hat{q}(k_x, k_z, y)]. \tag{F.7}$$

Filtering with $\mathcal{D}$ selects low-wavenumber (large lengthscale) up-gradient scales and results in the nonlinear flux plotted in Fig 16a. The complement $\mathcal{D}^c$ selects high wavenumber (small lengthscale) down-gradient scales that result in the nonlinear flux plotted in Fig 14a. We plot $\mathcal{D}$ for $y^+ = 100$ in Fig F.13a. Co-spectra resulting from filtering with $\mathcal{D}$ and with $\mathcal{D}^c$ are shown in Fig F.13c and Fig F.13d, respectively. These plots illustrate that the constructed filters separate the cospectrum into mainly down-gradient and up-gradient parts. The separation is not perfect, because of the graded nature of the filter kernel, but it was deemed sufficient for our analysis.

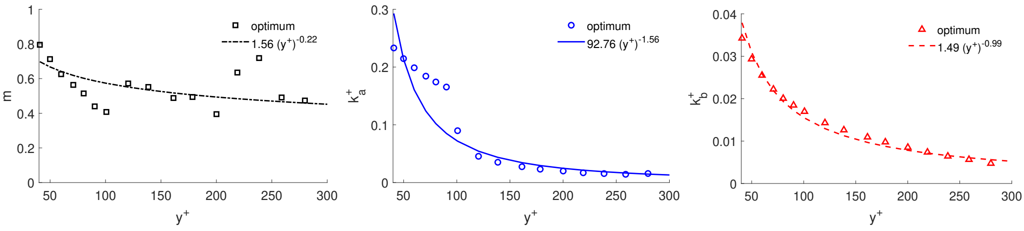

(a) (b) (c)

Figure F.12: Parameters of the Dragonfly filter $\mathcal{D}$ in the log layer. Points mark optimum values calculated by minimizing Σ^{U}_{yz}. Curves mark power law fits, which have been subsequently used to calculate the filter.

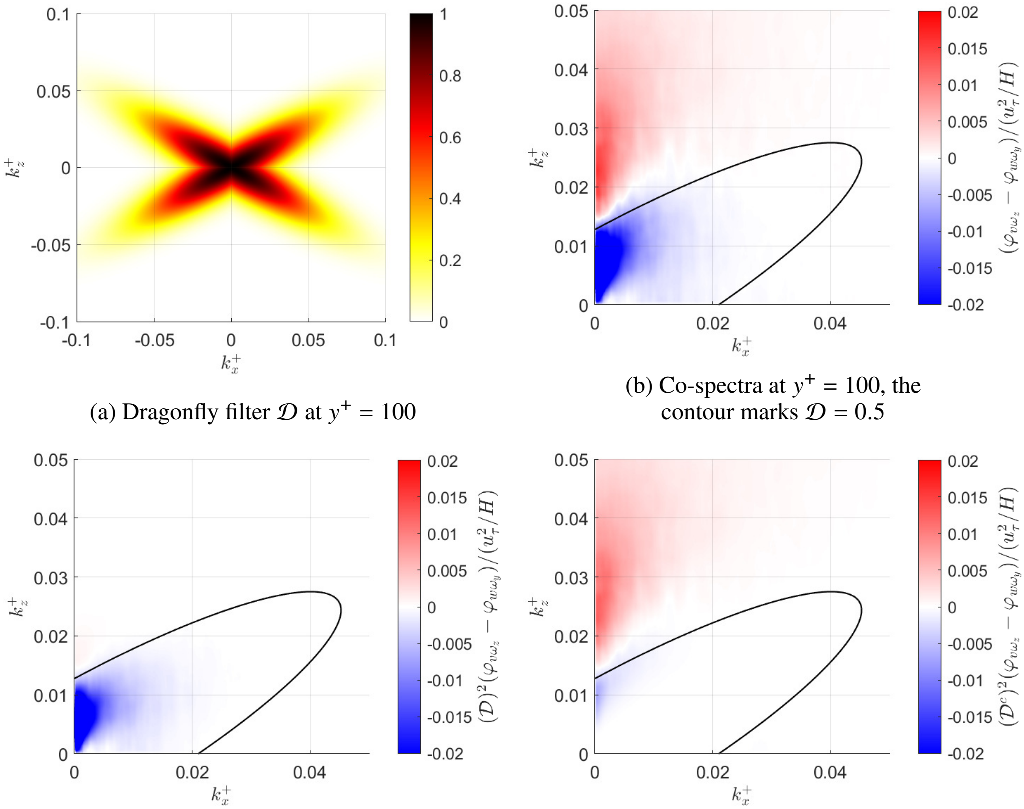

(a) Dragonfly filter $\mathcal{D}$ at $y^+ = 100$

(b) Co-spectra at $y^+ = 100$, the contour marks $\mathcal{D} = 0.5$

(c) Filtered co-spectra at $y^+ = 100$, the contour marks $\mathcal{D} = 0.5$

(d) Filtered co-spectra at $y^+ = 100$, the contour marks $\mathcal{D}^c = 0.5$

Figure F.13: Dragonfly filter and its application to the velocity-vorticity co-spectrum at $y^+ = 100$

G. Orientation of U-type vortices

We here present evidence that vorticity vector orientation within U-type vortices is predominantly spanwise and prograde, consistent with lateral stretching of pre-existing vorticity. This is demonstrated by Fig. G.14, which plots the same vortices visualized by the λ_2-criterion in Fig. 15 in the main text but coloured now by the cosine of the angle between vorticity vector $\boldsymbol{\omega}^U$ and the z-axis. We observe a prevalence of values smaller than -0.7, denoting prograde vortices forming angles smaller than $\pi/4$ with the z-axis. We note also the presence of a few retrograde vortices (shown in red) and a few which are not spanwise aligned (white).

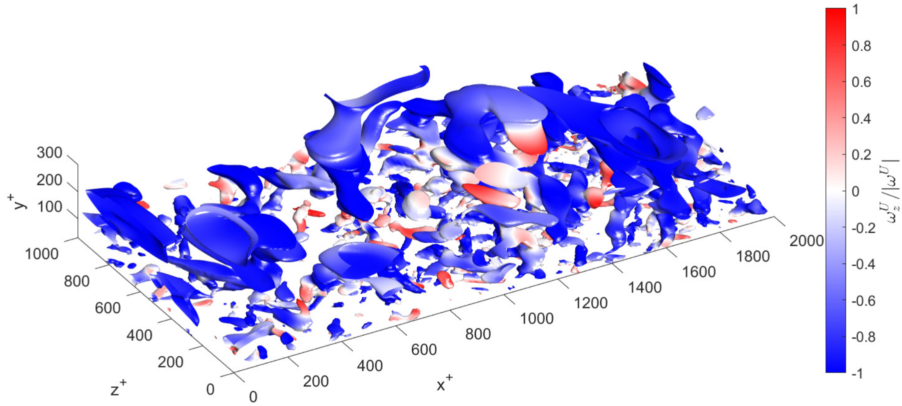

Figure G.14: Vortices identified using the λ_2-criterion for the velocity field $\mathbf{u}^U$ filtered using $\mathcal{D}$. Isosurfaces are plotted for $\lambda_2^U = -\lambda_2^{U,rms}$ and coloured by cosine of the angle made by the vorticity vector $\boldsymbol{\omega}^U$ with the z-axis, given by $\omega_z^U/|\boldsymbol{\omega}^U|$.